

# Investigation and Band Gap Analysis of Pulsed Dc Magnetron Sputtered Diamond-Like Carbon to Enhance Contact-Electrification and Durability of Triboelectric Nanogenerators

Ammara Ejaz, Michael McKinlay, Sam Ahmadzadeh, Manuel Pelayo Garcia, Lewis Fleming, Piotr Mazur, Michal Mazur, Des Gibson, and Carlos Garcia Nuñez\*

This work details the triboelectric characteristics of diamond-like carbon (DLC) film where a proportioned  $sp^3:sp^2$  bond ratio is engineered through a patented pulsed DC magnetron sputtering process to achieve a durable commercial energy harvesting material. A triboelectric nanogenerator (TENG) is fabricated by creating the triboelectric interface between DLC and PTFE. The presence and synchronization of  $\sigma - \sigma$  and  $\sigma - \pi$  bonds between DLC-PTFE contact surface amplify the electronic cloud overlap between their atoms leading to an enhancement of the triboelectric surface charge density. The inherent hardness and reduced friction achieved through DLC and PTFE respectively prevent the mass transfer, and consequent power loss upon consecutive mechanical contact and achieves a stable electric power output of  $141 \text{ mW m}^{-2}$ . The DLC durability achieved with PTFE in TENG demonstrates its significant potential as low frequency (1 – 10 Hz) energy harvesting devices and self-/low-power electronic devices and sensors. The paper uniquely contributes to a better understanding of the triboelectrification mechanism by insightfully detailing the band-to-band transition of electrons between the PTFE and DLC tribo-interface, as well as discussing gap and frequency limitation of the tribo-pair on the triboelectric charge yield, storage, transfer, and on the friction layer electric field.


## 1. Introduction

The topical concept of smart life through the deployment of autonomous electronic devices in every sector of life such as the Internet of Things (IoT), point-of-care health monitoring, smart buildings, manufacturing industry, etc., is timely and era-driven.<sup>[1]</sup> With a prediction of more than 100 billion interconnected devices worldwide in 2030,<sup>[2]</sup> it is imperative to find new ways to meet energy demands and harvest energy from existing resources in the environment to locally power the above technology. This can lead to the current autonomy for hours to reduce continuous reliance on battery charging and pollution caused by Li-ion batteries, contributing significantly toward the Net Zero Challenge.

In the last decade, scientists have revisited the exploration of the ancient phenomenon of triboelectrification to harvest mechanical energy otherwise

A. Ejaz, M. McKinlay, S. Ahmadzadeh, M. P. Garcia, L. Fleming, D. Gibson, C. Garcia Nuñez  
Institute of Thin Films  
Sensors and Imaging  
University of the West of Scotland  
Paisley PA1 2BE, UK  
E-mail: carlos.garcianunez@uws.ac.uk

L. Fleming, D. Gibson  
AlbaSense Ltd.  
Paisley PA1 2BE, UK  
P. Mazur  
Institute of Experimental Physics  
University of Wrocław  
Max Born 9, Wrocław 50-204, Poland  
M. Mazur  
Faculty of Electronics, Photonics and Microsystems  
Wrocław University of Science and Technology  
Janiszewskiego 11/17, Wrocław 50-372, Poland

 The ORCID identification number(s) for the author(s) of this article can be found under <https://doi.org/10.1002/admt.202300450>

© 2023 The Authors. Advanced Materials Technologies published by Wiley-VCH GmbH. This is an open access article under the terms of the Creative Commons Attribution-NonCommercial-NoDerivs License, which permits use and distribution in any medium, provided the original work is properly cited, the use is non-commercial and no modifications or adaptations are made.

DOI: 10.1002/admt.202300450

wasted in the environment (e.g., human motion, infrastructure vibration, mechanical triggering, rotation energy, wind, waves, etc.) and transform it into electricity.<sup>[3–6]</sup> This includes piezoelectricity,<sup>[7]</sup> triboelectricity,<sup>[8]</sup> electromagnetic induction,<sup>[9]</sup> etc., where triboelectricity has drawn more attention due to the off-shelf variety of low-cost materials, and a simple and portable design for wearable electronics.<sup>[8]</sup>

A simple design of a triboelectric nanogenerator (TENG) consists of two dielectric materials with opposite electron affinity. Based on the material's work function, a tribo-negative material extracts electrons from a tribo-positive material.<sup>[10]</sup> In 2012, a research group at Georgia Tech. led by Prof. Wang, discovered that the separation of these two dissimilar materials, produced an electrostatic effect, leading to the creation of energy.<sup>[3]</sup> Due to the relatively nascent TENG technology, it lacks insight into its various aspects, such as TENG's working mechanism, exotic tribo-pairing, device manufacturing, matching the high internal impedance of the tribo-materials with the external circuit, limited output current, post-stress conditions, and material transfer leading to low durability.<sup>[11]</sup>

Many efforts have been dedicated to coping with the aforesaid shortcomings of TENG devices through the structural design,<sup>[12]</sup> materials selection,<sup>[13]</sup> and surface charge density modification of the tribo-materials using ion etching<sup>[14]</sup> and imprinting.<sup>[15]</sup> Nevertheless, fewer efforts have been dedicated to optimizing the long-term durability of TENG materials. For example, TENG based on polymers such as PDMS,<sup>[16]</sup> PVDF,<sup>[17]</sup> and PET<sup>[17]</sup> have exhibited low friction, but are thermally unstable, soft in nature, and thus are not a viable option for industrial applications.<sup>[18]</sup> A TENG device exhibiting a remarkable thermal, chemical, and electrical stability, low friction coefficient, and electrically insulated would be an ideal material for commercial applications.<sup>[19,20]</sup>

Diamond-like carbon (DLC) films fill the gap perfectly due to an extended carbon network enriched with graphitic clusters linked by  $sp^2$  or  $sp^3$  bonding.<sup>[21]</sup> The relative amount of  $sp^2:sp^3$  dictates the physical properties, with electrical properties being dependent on the  $sp^2$ , and mechanical properties on the  $sp^3$  content.<sup>[22]</sup> In different deposition techniques,  $sp^3$  ( $\sigma$ ) and  $sp^2$  ( $\pi$ ) ratios can be tailored by optimizing the deposition conditions.<sup>[23]</sup> Moreover, it has been demonstrated that in H-free DLC, this ratio could strongly vary from surface to bulk.<sup>[24]</sup> In general, thin film materials are more uniform and have less defects in the bulk than on the surface. In the case of DLC, that indicates a low  $sp^3$  fraction (or low intensity D peak). In contrast, the surface of a thin film, typically presents dangling bonds, and impurities (hydrocarbons, gas species absorbed from the environment) making the  $sp^3$  fraction to be higher (i.e., larger D peak). However, there are some reports published in the literature,<sup>[24]</sup> that indicate the opposite behavior. In those works, H-free DLC was analyzed by surface-sensitive methods such as X-ray photoelectron spectroscopy (XPS) and X-ray absorption near edge structure (XANES), yielding smaller  $sp^3$  fractions (by up to 20%) than the bulk-sensitive techniques such as laser induced surface acoustic wave (LAwave) and Raman spectroscopy, being consistent with the assumption of a lower-density surface layer on a nominal-density bulk layer. It is worth noting, that only thicker films were able to show differences between bulk and surface characterization, sub-20 nm thin films exhibiting reasonable agreement be-

tween different surface and bulk techniques. In those studies, the deposition technique and specially the effect of the deposition rate were not discussed in depth and for that reason, further studies are needed to clarify their effects on the hybridization structures of DLC.

For an optimum TENG output power, low friction is desirable as low friction reduces the extent of adhesive interactions during periodic mechanical contact between TENG surfaces.<sup>[21,25]</sup> To avoid materials deterioration over time and loss of output power, the friction of the triboelectric films can be tuned by the introduction of the  $sp^2$  character.<sup>[21]</sup> A DLC film containing a proportioned amount of  $sp^3$  to achieve hardness, and  $sp^2$  to provide wearability through low friction would improve the electrical output and stability of the TENG devices. However, the nature of DLC films depends on various deposition parameters, such as substrate temperature, gas flow rate and ratio, plasma power, and residual pressure. It has been reported<sup>[26]</sup> that carbon films produced at low sputtering power (low deposition rate), the DLC films consisted mainly of  $sp^3$  bonds, while  $sp^2$  carbon ordering became dominant as the sputtering power increased. The  $sp^2/sp^3$  ratio of the carbon film controlled by the sputtering power is associated with two competing carbon deposition mechanisms: (1) collision between the incoming carbon ions and surface carbon atoms at low power (sub-plantation model) and (2)  $sp^3$ -to- $sp^2$  re-hybridization caused by the excess kinetic energy of the incoming carbon ions at high power (thermal relaxation). As the sputtering power increased, the friction, adhesion, and energy dissipation decreased, despite negligible topographical variations, while the conductivity rapidly increased but the deposition conditions can have a significant effect on the surface roughness of the deposited carbon-based layers.<sup>[26]</sup> Attaining these characteristics establishes the applicability of DLC as an exotic contact dielectric material for TENG applications.

DLC films are usually deposited through a pulsed vacuum arc discharge method,<sup>[27]</sup> hybrid plasma system,<sup>[28]</sup> femtosecond pulse laser deposition,<sup>[29]</sup> radio-frequency magnetron sputtering,<sup>[30]</sup> plasma enhanced chemical vapor deposition,<sup>[31]</sup> and pulsed DC-sputtering<sup>[32]</sup> using hydrocarbon or hydrogen-based feedstock. However, the use of hydrocarbon-based feedstock can negatively impact the TENG durability as the presence of hydrogen passivates the free electron dangling bonds and in turn density, hardness, Young's modulus, and compressive stress of the deposited carbon films.<sup>[33]</sup> In our previous study, we optimized the use of a pulsed DC-sputtered magnetron deposition system where hydrogen-free DLC films were deposited without the use of either a hydrocarbon or a hydrogenated feedstock.<sup>[33–36]</sup>

In TENG devices, a friction layer is typically composed of two materials with different electron affinities that are in contact with each other.<sup>[37]</sup> When the two materials rub against each other, electrons transfer from one material to the other, creating a potential difference between the materials. This potential difference can then be used to generate an electrical current in an external circuit. A maximum yield of tribo-charges upon contact and then translating them into electricity through electrostatic induction are directly proportional to the triboelectric charge density ( $\sigma$ ) on that friction layer, which in turn depends on the synchronization of the complimentary microstructure as contact materials.<sup>[38]</sup>

To complement the exotic characteristics of the DLC film, polytetrafluoroethylene (PTFE) would be the ideal and compatible

contact material to achieve the maximum output performance of a TENG device. PTFE is a chemically inert polymer, densely packed with two fluorine atoms bonded to each carbon atom, hydrophobic, carries high dielectric strength, and has the lowest coefficient of friction (0.05 – 0.10) of any known solid.<sup>[39]</sup> PTFE is often used to manufacture TENG modules in wearable flexible electronic devices due to fast charging time with high energy conversion efficiency, high output voltage, and stable characteristics.<sup>[40]</sup> PTFE being located at the negative end of the triboelectric series possess a strong ability to extract electrons and improve TENG's output performance.<sup>[41]</sup>

The nascent TENG technology is overwhelmed by shortcomings, especially the lack of insight into the triboelectrification mechanism and various factors influencing the output power performance of a TENG device. There is a wide gap in defining the storage and transfer mechanism of tribo- charges. Wang et al.,<sup>[42]</sup> sub-categorized the triboelectrification process into generation, storage, and dissipation of triboelectric charges. They introduced a composite structure in the friction layer to understand the storage mechanism of tribo-charges and discussed the function of carrier mobility and concentration in the charge-storing process to improve the TENG performance. The study insights on the storage position of the tribo- charges and their decay with time within the friction layer. However, it lacks information on the (1) yield of triboelectric charges (TCY) produced by the influence of different factors such as the gap between the contact materials, (2) frequency of the approaching contact material, (3) effect on the electric field by changing the gap between the contact material, and (4) time limitation to carrying out the charge transfer upon increasing frequency. Most importantly, (5) the band-to-band-transition of electrons among tribo-pairs during the electron transfer phase of triboelectrification has never been reported. Therefore, in this study, to the best of our knowledge, for the first time, we are going to insightfully discuss these 5 overlooked shortcomings of triboelectrification to contribute to a better understanding of the TENG mechanism and improve the designing of the device.

The study is using pulsed DC magnetron sputtering technique<sup>[34,35]</sup> to deposit highly uniform and compact DLC films from a non-hydrogenated feedstock to ensure the hardness and durability of the TENG device. XPS, Raman spectroscopy, and spectrophotometry were utilized to determine the  $sp^2:sp^3$  ratio and band gap energy in the DLC film respectively.

## 2. Results and Discussion

### 2.1. Spectroscopic Analysis of DLC Films

**Figure 1a** represents the pulsed DC magnetron sputtering system used to deposit a DLC film. The detailed deposition process with the optimized parameters is discussed in Section 4.1. **Figure 1b** shows the Tauc's plot obtained from the transmission and reflection measurements of the DLC films analyzed at incident photon energies ( $h\nu$ ) ranged between 0.44 to 0.49 eV. The optical band gap of DLC film was obtained by a plot of the absorption coefficient ( $\alpha$ ) against photon energy. The DLC film exhibited a Tauc's plot behavior with a direct band-to-band transition and a band gap energy ( $E_g$ ) of  $\approx 0.476$  eV. In amorphous DLC film, this  $E_g$  corresponds to the presence of  $\pi$ -bonded  $sp^2$  clusters as  $\pi$  states

lie closer to the Fermi level than the  $\sigma$  states.<sup>[43]</sup> The narrow band gap attained in DLC film identifies it as an interesting complementary material for a wide band gap PTFE material to intensify the built-in electric potential created within the friction layer. The higher built-in electric potential enhances the yield of triboelectric charges and consequent electric current through external circuits.<sup>[44]</sup>

**Figure 1c** shows the deconvoluted XPS spectrum of DLC film. The C1s photoelectron spectrum was decomposed into four peaks with two peaks of binding energies (BE) at 284.8 and 285.9 eV corresponding to  $sp^2$ -C (C = C), and  $sp^3$ -C (C - C) hybridized states.<sup>[45]</sup> The ideal graphite  $sp^2$  peak of C1s spectrum exhibits 284.5 eV, however, the 0.2 eV blue shift in the high BE side of  $sp^2$ -C is attributed to the samples containing a high amount of diamond which is influenced by the charging effect of diamond C  $sp^3$  domains.<sup>[46]</sup> The *ex-situ* transfer of material from one system to another exposed DLC film to air oxidation resulting in the generation of two additional secondary oxidation peaks corresponding to the presence of C - O - C, and O - C = O at 287.6 and 290.4 eV respectively.<sup>[47]</sup> The spectrum shows a weight percentage of 9.24% of  $sp^2$ -C, and 72.05% of  $sp^3$ -C, as well as 15.37% and 3.33% corresponding to secondary oxidized carbons in the DLC film. As discussed above, the  $sp^3$  configuration is dominant at a low sputtering power of 15 kW, the  $sp^2$  ordering gradually increases as the sputtering power increases up to 30 kW,<sup>[26]</sup> herein the utilization of 4kW power to obtain DLC-deposited films complements our XPS analysis where the DLC surface is enriched with  $sp^3$  content as per deposition parameters.

Literature accounts that the values of BE separation are dependent on the structural disorder, defects, oxygen, and hydrogen content of the material<sup>[48]</sup> and a significantly lower BE level for broad core-level  $sp$ -allotrope, relative to BE for elemental carbon contributions toward DLC film.<sup>[49]</sup> The fitted  $sp^3$  and  $sp^2$  constituents defined the energy separation gap between their BE ( $\Delta BE = BE_{sp^3} - BE_{sp^2}$ ) in accordance with the previous reports.<sup>[50-54]</sup> The BE separation value between  $sp^2$ -C and  $sp^3$ -C has been reported as 0.6 eV<sup>[50]</sup> and 0.8 eV<sup>[51]</sup> for hydrogen free-DLC films, 0.7 eV for graphene oxide,<sup>[52]</sup> 0.9 eV for graphite,<sup>[53]</sup> and 1.3 eV for onion like diamond.<sup>[54]</sup> In this work, sputtered DLC films showed a  $\Delta BE$  of  $\approx 1.1$  eV (**Figure 1c**).

**Figure 1d** represents the Raman analysis carried out to identify the characteristic D and G bands in the DLC film, which correspond to  $sp^3$  and  $sp^2$  bonds, respectively.<sup>[55]</sup> Deconvolution of Raman peaks through Gaussian peaks fitting emerged with two peaks the G band at  $1536.39\text{ cm}^{-1}$  and D band at  $1333.9\text{ cm}^{-1}$ . These results are in good agreement with previous studies reported in the literature, showing the emergence of the G position in the spectrum range of  $1528 - 1539\text{ cm}^{-1}$ .<sup>[56]</sup> Herein, the significant emergence of D band in the Raman spectra suggests the transition of ideal graphitic  $sp^2$  network to disordered graphitic vibrations ( $sp^3$ ) during the pulsed DC magnetron sputtering deposition. The  $I_D/I_G$  ratio was calculated from the D and G band intensities and was found to be 0.457 suggesting 45.7% of  $sp^3$  and 54.3% of  $sp^2$  content in the DLC film. Further to this, a well-accepted method published by W.G. Cui et al.<sup>[57]</sup> where a theoretical expression describing the correlation between  $sp^3$  content and FWHM of the G peak obtained in Raman measurements in

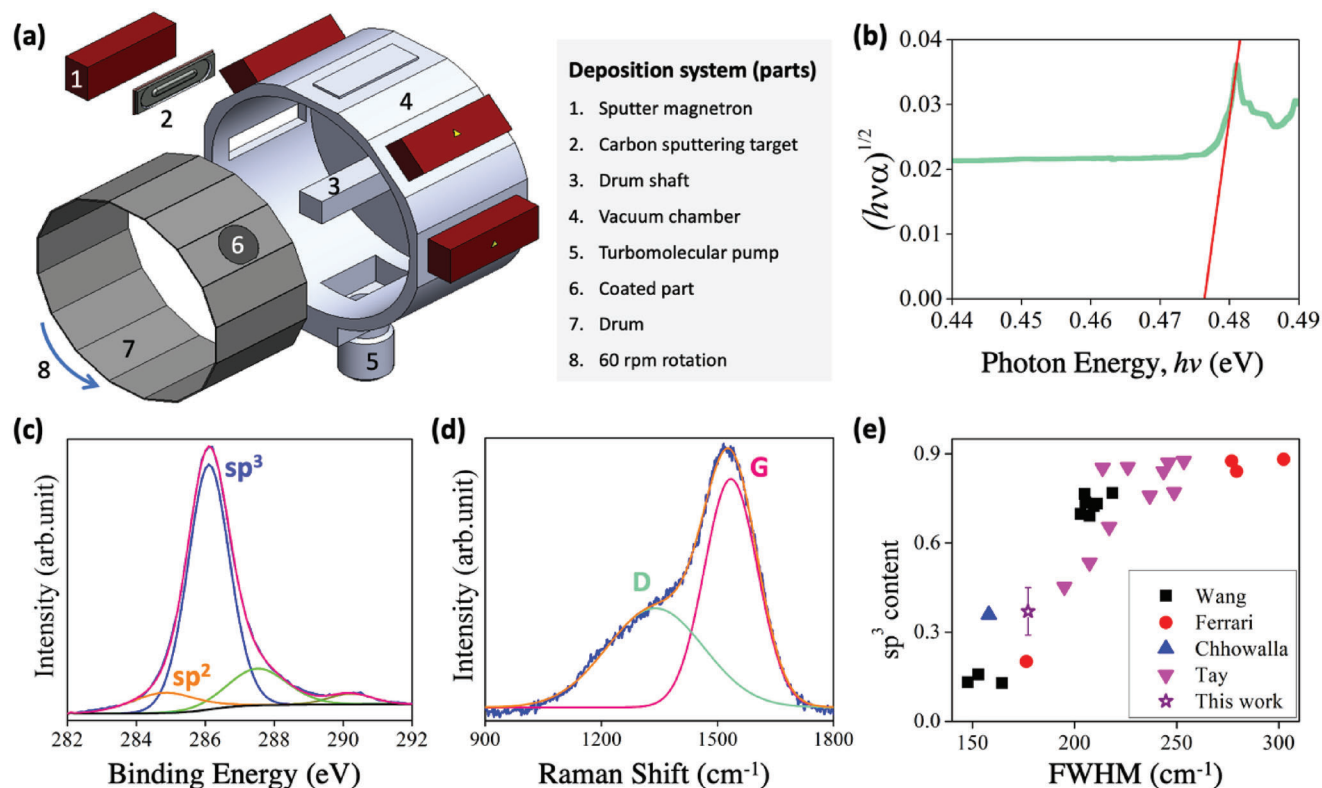


**Figure 1.** a) The 3D schematic diagram of the pulsed DC magnetron sputtering system used to deposit the DLC films. b) Tauc's plot of the amorphous DLC film. c) Deconvoluted C1s XPS spectrum of DLC, exhibiting 9.24% of C = C, 72.05% of C – C, 15.37% of C – O – C, and 3.33% of O – C = O weight percentage. d) Raman spectrum of DLC, showing D band related to  $sp^3$  bond (@1333.9  $cm^{-1}$ ) and G band related to  $sp^2$  (@1536.39  $cm^{-1}$ ); e) a correlation between  $sp^3$  content and FWHM of Raman G peak measured in H-free DLC film of our sample and deposited by different research groups.<sup>[57–63]</sup>

H-free DLC was used to calculate the  $sp^3$  content obtained in our DLC sample. The mathematical expression is as follows:

$$sp^3 \text{ content} = -2.05 + 0.019 W - 3.01 \times 10^{-5} W^2 \quad (1)$$

Where  $W$  is calculated from the FWHM of G peak measured at an arbitrary excitation wavelength  $\lambda$ .

$$W = FWHM(G \text{ peak @ } \lambda) + 0.21(514 - \lambda) \quad (2)$$

This empirical expression was obtained by using a series of experimental results published by various research groups<sup>[57–63]</sup> on H-free DLC films deposited using different techniques.

To use the above expressions, we calculated the FWHM of our G peak obtained at  $\lambda = 532$  nm. That FWHM @ 532 nm resulted in 159  $cm^{-1}$ . First, we plugged that value into Equation (2), obtaining a  $W$  of 177.21  $cm^{-1}$ ; then, the resulting  $W$  was plugged into Equation (1) to estimate the  $sp^3$  content of our samples, resulting in an  $sp^3$  content of  $37\% \pm 8\%$ . For the sake of comparison, we have also plotted in Figure 1e, this result along with those reported in literature.<sup>[57]</sup>

This calculated  $sp^3$  content from the mathematical expression above is also complementing the  $sp^3$  content obtained by Lee et al.,<sup>[26]</sup> where the research group prepared three DLC films with different sputtering powers of 15, 20, and 30 kW. The Raman

spectra @ 532 nm of these films were recorded with D and G peaks at  $\approx 1400$  and  $\approx 1570$   $cm^{-1}$  respectively. This Raman analysis concluded that as the sputtering power increases from 15 to 30 kW,  $I_D/I_G$  increases from 0.74 to 1.56, and the G peak is blue-shifted from 1569 to 1572  $cm^{-1}$ , indicating a phase change from a-C to  $sp^2$ -rich graphite-like phase.<sup>[64]</sup> The reduced FWHM of the G peak implies an enhanced  $sp^2$  ordering of carbon with increased sputtering power. The stiffened vibration modes indicate that  $sp^2$  clustering dominates because of a reduction in the topological disorder of  $sp^2$  carbons as the sputtering power increases.<sup>[64]</sup> It is interesting to note here that for our DLC film we utilized 4kW sputtering power and by extra plotting the results of Lee et al., from 15 to 30 kW, our  $I_D/I_G$  ratio ( $37\% \pm 8\%$ ), the peak position of G (1536.39  $cm^{-1}$ ), and FWHM (159  $cm^{-1}$ ) follows the same trend. The analysis suggests a significant proportion of both  $sp^2$  and  $sp^3$  characters which are the desired characteristics of the material, required to obtain a high-power stable, and durable TENG device.

From the spectroscopic analysis, it is interesting to observe that the percentage of  $sp^2:sp^3$  ratios identified by XPS and Raman analysis are different. This result is due to XPS being a surface technique and average depth analysis for XPS measurement is  $< 10$  nm,<sup>[65]</sup> whereas Raman imaging is  $< 1$   $\mu m$  in diameter,  $< 10$   $\mu m$  in depth.<sup>[66]</sup> Hence the difference in weight percentage. The presence of a higher  $sp^3$  content on the surface of DLC film from

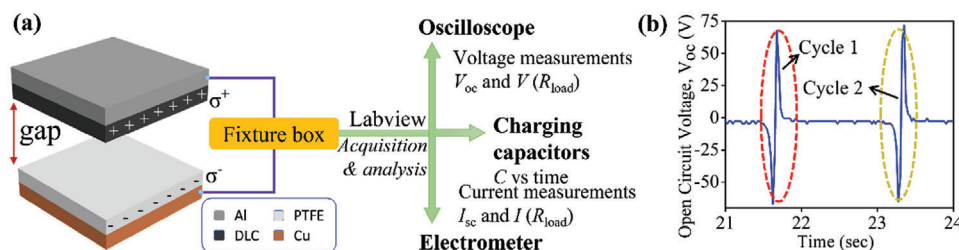


**Figure 2.** a) A schematic diagram of the home-made automatic actuation system to electrically characterize TENG devices. TENG devices based on DLC (tribopositive) and PTFE (tribonegative) with Al and Cu as electrodes. Surface charge density ( $\sigma$ ) indicated in the diagram. Customized fixture box utilized to measure voltage, and current produced by TENG, as well as charging characteristics of energy storage devices (e.g., capacitors). b) Two AC signals obtained at 0.5 Hz frequency with a 70 mm gap between the DLC and PTFE tribo-materials.

the XPS analysis indicates the extraordinary hardness of DLC film to contribute to the stability of the TENG device through periodic mechanical contact-separation cycles. The significant presence of  $sp^2:sp^3$  ratios achieved in bulk through Raman and XPS analysis suggests the uniqueness of the DLC film to attain desired low friction from the  $sp^2$  character and improve electrical output and achieve durability through  $sp^3$  hardness in a TENG device.

## 2.2. Electrical Characterization of DLC-PTFE based TENG Device

The triboelectric effect formed between DLC-PTFE friction layer was examined by varying a wide range of contact-separation frequencies, and gap distances between electrodes to obtain the maximum power output from the device. For that, a home-made automatic actuation system was built to characterize the open-circuit voltage ( $V_{oc}$ ), short-circuit current ( $I_{sc}$ ), output power ( $P_{out}$ ) for different load resistances ( $R_{load}$ ), as a function of aforementioned contact-separation conditions (Figure 2a). Moreover, the use of fixture box and an interface programmed in LabVIEW, allowed to test the TENG as an energy source to charge capacitors and drive external loads, e.g., sensors, LEDs, etc. Further details about the system could be found in Section 4.

Figure 2b shows a thorough view of two full cycles consisting of triboelectric materials contacting and separating with an approaching frequency of 0.5 Hz and 70 mm gap. It is noteworthy to understand here that for triboelectricity, the electron affinity of a material defines its extent to gain or lose electrons.<sup>[67]</sup> As such the PTFE is highly electronegative compared to DLC. For electrical characterization, as shown in Figure 2a, a *face-to-face* configuration was established, where a Cu electrode was attached to the PTFE dielectric material, and DLC film was directly deposited on an Al foil (Al serving as a second electrode). Upon contact electrification, dielectric materials are charged due to the difference in their electron affinities, PTFE being highly electronegative and having higher work function<sup>[41]</sup> exhibits a higher tendency to extract and accept electrons from DLC film, leaving a positively charged DLC surface.

Before going into the mechanism of triboelectrification, generally, upon contact between both tribo-interfaces, the cloud of generated triboelectric surface charges remains on both dielectric materials, i.e., PTFE and DLC film even on separation. This charge accumulation on the surface of dielectric materials is conventionally defined as  $\sigma$  (or  $\sigma_T$ ) and causes the generation of a

surface potential difference. Upon separation of materials by a certain gap (Figure 2a), this potential difference in turn creates an electric field that ultimately drives the transfer of electric charges from one electrode to another through an external circuit (see purple wire in Figure 2a). Upon the completion of a single contact-separation cycle, the dielectric materials again come in contact, the electric field disappears, and the electrons move back to the respective materials. This whole phenomenon results in the generation of an AC electric signal<sup>[3,8]</sup> as shown in Figure 2b. From that Figure, one could conclude that the AC signal is not symmetric (i.e., the intensity of the electric field), indicating that the separation and approaching steps in TENGs depends on the electro-positive and electronegative material. In this particular TENG based on DLC-PTFE, the  $V_{oc}$  reached upon separation is lower ( $\approx 60$  V) than that observed during the approaching step ( $\approx 75$  V). In spite of this asymmetric behavior, the fact that both steps produce similar levels of  $V_{oc}$  making this TENG compatible with single electrode mode configuration.<sup>[68]</sup>

Investigation of the mechanism explains triboelectrification as a multistep procedure (Figure 3) which we are breaking down into two main phenomena, comprising: (i) charge transfer between triboelectric materials upon contact electrification, and (ii) charge compensation from the electrodes under the influence of created electric field upon releasing. In Section (i) of the triboelectrification, we are going to detail the charge generation profile upon contact, the atomic overlap between the contact materials (Figure 3a–c), and electron transfer between the PTFE and DLC film through a band-to-band transition (Figure 3d–f). Whereas section (ii), i.e., charge compensation through the influence of electric field will be explained from charge storage on the triboelectric interfaces, the intensity of the depletion region under the influence of gap and frequency of the approaching contact material, and finally the charge transfer through the created electric field (Figure 3g–i).

(i) *Charge transfer between triboelectric materials upon contact electrification:*

Figure 3a–c shows the 3D schematics of the PTFE and DLC film before any contact, electronic distribution in C atom (DLC) and F atom (PTFE), and band energy diagram of PTFE and DLC film, respectively. DLC has moderate electron affinity, illustrated in Figure 3c, with a conductive band energy level ( $E_C$ ) right above the vacuum level ( $E_{vac}$ ). In this scenario, electrons promoted from the valence band ( $E_V$ ) to the  $E_C$  in DLC will be able to be transferred to an electronegative material, e.g., PTFE. PTFE is an organic material, whose energy bands could be expressed as LUMO

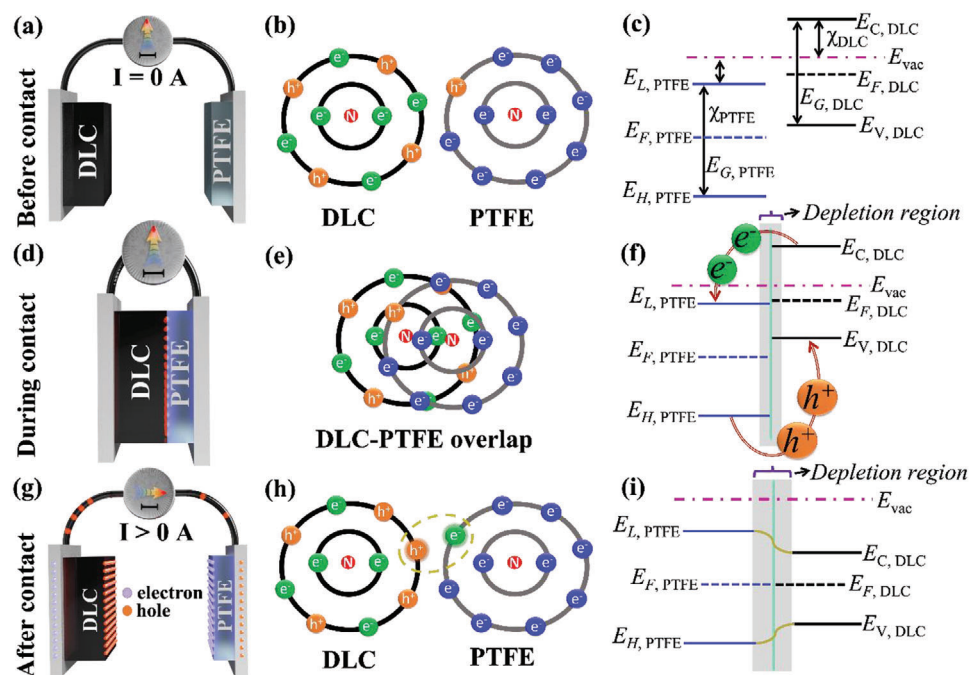


**Figure 3.** Before contact electrification PTFE and DLC films a) the 3D schematics, b) an atomic-scale charge transfer mechanism with shell diagram of C atom in DLC and F atom in PTFE tribo-materials, and c) the energy band gap diagram in ground state. During contact electrification through the external mechanical force between the PTFE and DLC film d) the 3D schematics, e) the electronic cloud overlap, and f) formation of depletion region and band-to-band transition of electrons and holes from DLC to PTFE and vice versa. After separation of PTFE and DLC tribo-interface g) the 3D schematics exhibiting abundance of electrons on PTFE and holes on DLC surface, h) the shell diagram of electron extraction of PTFE from DLC film, and i) the heterojunction formed between the PTFE and DLC film at equilibrium.

( $E_L$ ) and HOMO ( $E_H$ ), and they are equivalent to the  $E_C$  and  $E_V$  of an inorganic semiconductor (Figure 3c). The position of the  $E_L$  in PTFE is slightly below the vacuum level, which makes this material has a higher electron affinity than the DLC. In other words, the fact that electrons in the  $E_C$  of DLC are located at energy levels above the  $E_{vac}$ , makes them weakly attracted by the DLC material and thus highly attracted by PTFE.

As can be seen in Figure 3a, no electric current was passing through the external circuit prior to the first contact, mainly due to absence of  $\sigma$ . However, when the external force was applied to generate contact electrification (Figure 3d), PTFE and DLC atoms get closer to each other, and the electronic cloud of both tribo-materials starts to overlap due to the decrease in their interatomic distance (Figure 3e). This generated a repulsion between the PTFE and DLC atoms and causes a drop in the energy barrier between the PTFE and DLC, resulting in electron transfer,<sup>[69]</sup> i.e., the generation of triboelectric charge density on PTFE and DLC surfaces (tribo-interfaces). It is in this region that electron transfer occurs. As mentioned above, this electron transfer from DLC film to the PTFE is attributed to the low electron affinity and higher work function of the PTFE.<sup>[70]</sup>

To understand the mechanism of electron transfer between the DLC film and PTFE materials, Figure 3f shows a detailed band gap diagram with band-to-band transitions of electrons between the PTFE and DLC film during contact electrification. At an atomic scale, the charge transfer depends on the nature of the heterojunction formed between the DLC and PTFE contact interface. As we know, the electrons filled in lower energy band gaps

move to a higher energy band by absorbing energy. These excited electrons eventually return to their original lower energy state by releasing the excess energy as heat or light.<sup>[71]</sup> The electron affinity of a material is critical in determining its band gap, and it can affect both the size and the position of the band gap. Due to the lower electron affinity of the PTFE, the electrons are inclined to move from a lower energy band gap (DLC) to a higher energy band gap (PTFE) upon charge generation from the initial contact of the tribo-interface. The electric field created between the PTFE and DLC drives electrons from a low to a high energy level by doing work on the electron and increasing its potential energy.<sup>[44]</sup> Herein, as shown in Figure 3f, the electrons and holes moved in the opposite direction from a low to a high energy level and vice versa and completes the charge transfer between the DLC film and PTFE.

As can be seen in Figure 3g, due to the transfer of electrons from DLC film to the PTFE, the PTFE surface is in an abundance of electrons whereas, DLC is left with the holes. Figure 3h demonstrates this atomic scale transfer of electron from DLC film to the PTFE with the formation of an ionic bond.

(ii) *Charge compensation from the electrodes under the influence of an electric field:*

The electron transfer from the DLC film to the PTFE material in section (i) creates a potential difference that leads to the formation of a depletion region between the PTFE and DLC tribo-interfaces.<sup>[44,72]</sup> Figure 3f,i shows a varied thickness of depletion region created upon contact electrification. The surface charge accumulation on tribo-pairs (Figure 3g) creates a dual-mode

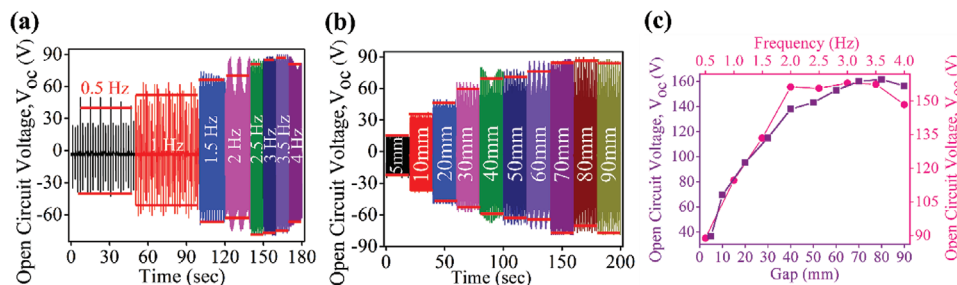


**Figure 4.** AC signals recorded between DLC and PTFE tribo-interface from the a) effect of different frequencies from 0.5 to 4 Hz at 70 mm gap. b) Effect of gap from 5 mm – 90 mm between approaching DLC and PTFE at 3 Hz frequency. c) Statistical analysis of effect of gap and frequency between the DLC and PTFE dielectric materials with respect to their output AC signal.

electron transfer, either through diffusion where the creation of a concentration gradient induces complementary charges into the Cu and Al electrode or through the drift process by the introduction of an electric field between PTFE and electrodes.<sup>[42]</sup> This dual electron transfer mode eventually drives the electron into the external circuits and generates an AC signal as shown above in Figure 2b,g. The dual-mode electron transfer in TENG is highly dependent on the characteristics of the vibration source, including amplitude (gap between the tribo- materials) and frequency, as we will demonstrate experimental later on.

To explore and validate DLC films as tribo- material in TENG, the output electric signal of PTFE-DLC based TENG was recorded at various frequencies. **Figure 4a** shows  $V_{oc}$  obtained from 0.5 to 4.0 Hz with a gap of 70 mm between DLC film and PTFE dielectric materials. The AC signal showed an increment in  $V_{oc}$  from 88.77 to 157.92 V with an increase in frequency from 0.5 to 3.0 Hz. As shown in Figure 3f,i a varied thickness of depletion region is created upon contact electrification. This is because the depletion region thickness depends on the frequency of the TENG device. At low operating frequency, the low charge density is transferred between the tribo- materials which in turn creates a smaller potential difference and a narrow depletion region (Figure 3f). However, at a higher frequency, the significant transfer of triboelectric charge density creates a wider depletion region (Figure 3i), hence higher  $V_{oc}$ . However, after exceeding 3.0 Hz, frequencies of 3.5 and 4.0 Hz started to show a decline in the  $V_{oc}$  with 157.40, and 148.34 V respectively (Figure 4a). This decrease in output performance for a higher frequency suggests the accumulation of a higher triboelectric surface charge and insufficient time to complete the transfer of electrons through the external circuit and exhibited a lack of replenishing the electrode surface with fresh surface charge density upon next contact. This means that the presence of tribo-charges on contact surfaces seems to have blocked the path for the new charges to be accumulated on the surface, hence the decrease in  $V_{oc}$ .

The gap between both dielectric materials is another optimization key to obtaining the maximum power output of PTFE and DLC tribo-pair, as the electric field created upon the separation of each dielectric depends on the distance between approaching materials.<sup>[73]</sup> A thorough study with a gap from 5 to 90 mm was tested between DLC film and approaching PTFE to assess the sufficient timeframe and consequent maximum transfer of electrons through the circuit. The AC signal showed an improvement in its response until the 70 mm gap with an increment of AC

signal from 36.59 to 160.14 V, however, a further increase to the 80 mm gap contributed a slight increase (161.68 V) of voltage for that magnitude of gap increase between both dielectric materials. A 10 mm further increase in gap, i.e., the gap of 90 mm exhibited a decrease in AC signal with a  $V_{oc}$  value of 156.42 V, signifying the gap limitation between DLC and PTFE material (Figure 4b). As discussed in Figure 3g, the surfaces charge accumulation on tribo-pairs creates a dual-mode electron transfer, (i) through diffusion where the creation of a concentration gradient induces complementary charges into the Cu and Al electrode, and (ii) through drift process by the introduction of an electric field between PTFE and electrodes.<sup>[42]</sup> Herein, the drop observed in the  $V_{oc}$  on increasing the gap from 70 mm onwards is attributed either to the adsorption of positively charged ions or particles from the air or the recombination of triboelectric charges with the induced complementary charges on the electrode.<sup>[42]</sup> The  $V_{oc}$  drop on increasing the gap from 70 mm between the approaching electrodes can also be caused by the air breakdown.<sup>[74–76]</sup> By understanding the phenomenon of air breakdown during the triboelectrification and electrostatic induction, the breakdown effect will cause surface charge loss and then decrease the induced charge density as triboelectric charges are released by air breakdown before they can be completely induced in the external circuit, so the induced charges generally are smaller than real triboelectric charges. Over a 70 mm gap between the approaching electrode, a certain competing relationship between electrostatic induction and electrostatic breakdown exists.

It is worth noting that triboelectric charges may also cause the ionization of the atmosphere and attract opposite charges in the atmosphere with trace amounts and slow speeds rather than spark discharge through the external circuit.<sup>[74–76]</sup> These outcomes conclude the crucial optimization of time to maintain these accumulated surface charges on tribo- interfaces and prevent their recombination with the charges generated by the electrode, avoid a competition with air breakdown, and atmospheric ionization to avoid their decay and loss of triboelectric charge density. Therefore, a liaison between the gap of the approaching contact surface and frequency must be aligned to obtain the maximum output performance of a TENG device.

Figure 4c shows the statistical analysis derived from the output AC signals with respect to the varying frequencies and gaps (Figure 4a,b). As concluded above, Figure 4c shows the maximum output performance with a combination of 3.0 Hz operating frequency at an optimum gap of 70 mm between approaching

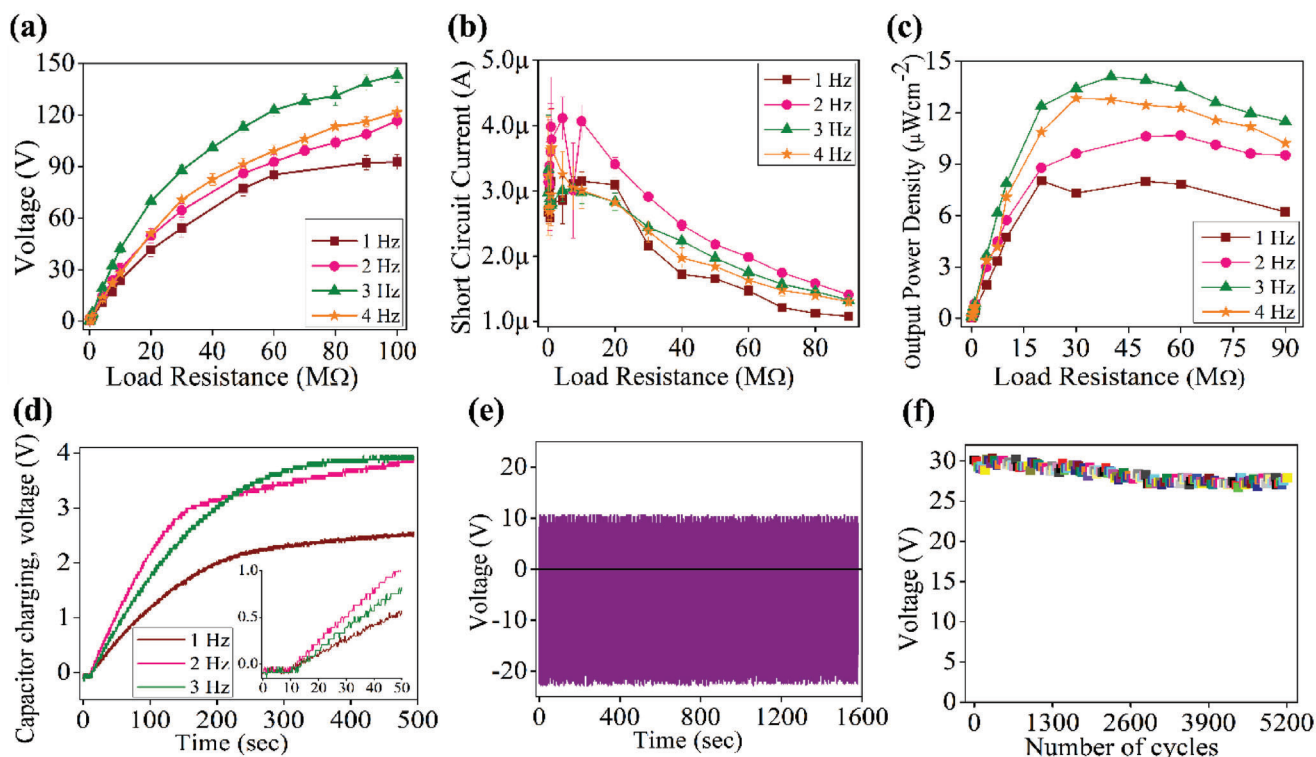


**Figure 5.** The statistical analysis DLC-PTFE TENG output characteristics, including: a) voltage, b) current, and c) power density vs.  $R_{load}$  ranged between 56 k $\Omega$  to 100 M $\Omega$  for various frequencies (1 – 4 Hz). d) Charging curve of a 3.3  $\mu$ F capacitor obtained using a TENG operated at different frequencies (1 – 3 Hz). e) TENG voltage obtained at 3 Hz and recorded for long-term stability using a  $R_{load}$  of 1 M $\Omega$ . f) TENG voltage vs. number of contact-separation cycles; extracted from (e). All the experiments in this figure have been conducted using a gap of 70 mm.

dielectric materials. Based on these two findings, all experimental electrical analyses were carried out with a 3.0 Hz frequency and a gap of 70 mm between PTFE and DLC tribo-pair.

Next on, the DLC-PTFE TENG performance was analyzed to match the internal impedance of the tribo-pair with different load resistors, aiming to enhance the TENG output power and to improve its integrability with external circuits. For this purpose, a TENG device with a surface area of 4cm<sup>2</sup> was used to harvest energy from a vibration source with a frequency ranging from 1 – 4 Hz and an amplitude of 70 mm. Figure S1(a–d) (Supporting Information) presents the voltage dropped across a  $R_{load}$  with resistances ranging from 56 k $\Omega$  to 100 M $\Omega$ . For the sake of clarity, the inset of each Figure S1(a – d) (Supporting Information) shows the  $R_{load}$  voltage drop obtained at the of TENG generated a lowest applied  $R_{load}$ , range of  $R_{load}$  (i.e., in k $\Omega$ .k $\Omega$ ). After each measurement, the  $R_{load}$  was changed, multiple readings were recorded corresponding to each  $R_{load}$  and an experiment was performed with the same protocol for each frequency (1 – 4 Hz). Figure S1(a – d) (Supporting Information) evidences the increase of the TENG voltage with the  $R_{load}$  independently on the operating frequency, exhibiting small augmentation of the voltage at low  $R_{load}$  (see inset of Figure S1, Supporting Information), and maximum voltages of 143.33 V for  $R_{load}$  of 100 M $\Omega$  (Figure S1c, Supporting Information). This maximum voltage implies a 90.7% extraction of the voltage observed in open-circuit configuration (Figure 4a) at 3 Hz among all frequencies. Another characteristic observed in Figure S1 (Supporting Information) is the

improvement of the AC signal symmetry with respect to the 0 V level. Compare to the low  $R_{load}$  (see inset of Figure S1(a–d) (Supporting Information)), the higher  $R_{load}$  range exhibited a more symmetric AC signal which is desirable when using TENG as an electronic component in circuits (e.g., signal rectification, AC circuits, power management modules, etc.).

Short-circuit current ( $I_{sc}$ ) of the TENG device was analyzed as a function of  $R_{load}$  and for various frequencies ranging from 1 – 4 Hz, keeping the contact-separation gap distance between tribo- interfaces at 70 mm (Figure S2, Supporting Information). Figure S2(a–d) (Supporting Information) shows the current dependency of the tribo- device on the applied  $R_{load}$ , the lower  $R_{load}$  extracted a higher current as compared to the higher applied  $R_{load}$ . The increases of the voltage and decrease of the current in our TENG devices with  $R_{load}$  is in good agreement with previous output characteristics reported in the literature.<sup>[77]</sup>

For the sake of comparison, TENG output voltage and current obtained from Figures S1 and S2 (see Supporting Information) have been plotted against applied  $R_{load}$  in Figures 5a,b, respectively. Figure 5a, shows that TENG output voltage increased with  $R_{load}$ , exhibiting a linear relationship between both magnitudes for low resistances, and sublinear behavior for a higher range of resistances. The V intends to saturate above a certain value of  $R_{load}$ , the latter being characteristic of the vibration source (gap and frequency). In contrast, the TENG output current exhibited the reverse trend (Figure 5b), i.e., it decreases as the  $R_{load}$  increases. This decrease in the current could be easily



understood by using Ohm's laws (i.e., the current of a conductor is inversely proportional to its resistance). As the external load resistor value increases the voltage drop across the resistor increases (Figure 5a), which reduces the output current. The obtained analysis in both Figures 5a,b agrees well with the observations in Figures S1 and S2 (see Supporting Information) which are complementing Ohm's law.

Finally, the  $P_{out}$  of the TENG was calculated by multiplying the voltage dropped across a  $R_{load}$  in Figure S1 (Supporting Information) as a function of the current flowing through the resistor (Figure S2, Supporting Information). The statistical analysis in Figure 5c concludes the maximum output power density of  $141 \text{ mW m}^{-2}$  at  $40 \text{ M}\Omega$   $R_{load}$  at a 3 Hz frequency (with a gap of 70 mm). The remarkable output power density of the TENG device is credited to a high proportioned  $sp^2$  character in the DLC film which reduces the friction with the PTFE interface upon contact and thus escalated the charge transfer. Furthermore, one could conclude that the maximum  $P_{out}$  is reached when the internal impedance of TENG matches the external impedance of the circuit, i.e., the  $R_{load}$  and the wires used to connect the component to the TENG. Moreover, it is worth noting, that TENG's maximum output power density varies with the frequency, at 1 Hz, the PTFE- DLC tribo- pair generated a maximum output power density of  $80.3 \text{ mW m}^{-2}$  at  $20 \text{ M}\Omega$ , at 2 Hz it exhibited  $101.3 \text{ mW m}^{-2}$  at  $70 \text{ M}\Omega$ , and 4.0 Hz presenting  $128.5 \text{ mW m}^{-2}$  at  $30 \text{ M}\Omega$ . This result is well understood, since the impedance of the circuit working in AC, strongly depends on the frequency of the input signal, in this case, the TENG.

The output characteristics of TENG devices fabricated here, demonstrated output currents in the range of  $\mu\text{A}$ , and  $P_{out}$  in the range of hundreds of  $\text{mW m}^{-2}$ , making them promising energy sources to power energy storage devices. In this regard, TENG devices developed in this work were successfully utilized as energy harvesters to power small energy storage devices. Figure 5d shows the characteristic charging curves of a  $3.3 \mu\text{F}$  capacitor, charged by using a TENG device operated at 1, 2, and 3 Hz with an approaching gap of 70 mm and with the circuit described in Figure 2a to convert the AC signal of the TENG into a DC signal. As can be seen in Figure 5d, a saturated voltage ( $V_{sat}$ ) of 2.8, 4.01, and 4.6 was achieved for 1, 2, and 3 Hz frequencies, respectively. From these values of  $V_{sat}$ , the time constant  $\tau$  of the capacitor was calculated for TENG frequency. At 1 Hz frequency, the capacitor took 154 s to reach its 66.67% charging, however, at 2 Hz frequency there was a reduction of 30 seconds to reach the same  $\tau$  and a further increase in frequency, i.e., 3 Hz showed a decrease of 8 seconds with respect to the 2 Hz to acquire the same voltage ( $\tau$ ).

Further on, the durability of the TENG was evaluated by subjecting the devices to over 5,000 contact-separation cycles. For this study, the same optimized experimental protocol (frequency = 3 Hz, gap between the PTFE and DLC = 70 mm, and  $R_{load}$  =  $10 \text{ M}\Omega$ ) in a contact-separation mode were applied. Figure 5e presents the results of the stability study, where one can observe a stable  $V_{oc}$  over a period of 30 min. The level of retention in the positive (+10 V) and negative (-25 V) peak voltage for over 5,000 cycles (Figure 5f), confirming the good stability of the material, and negligible transfer of DLC film into the PTFE surface, the latter typically observed in TENG devices operating for long periods. This incredible stability of the TENG device is credited to the

presence of a higher hydrogen-free  $sp^3$  content of the DLC film achieved through pulsed DC magnetron sputter deposition.

### 3. Conclusion

The paper discusses a novel approach to achieving a durable DLC film for the commercial, high-volume production of energy harvesting devices by optimizing a hydrogen-free  $sp^3$  content through the pulsed DC magnetron sputter deposition technique. The tribo- interface created between DLC film and PTFE exhibited extraordinary long-term durability through continuous over 5000 contact-separation triboelectric cycles with a maintained almost the same voltage across  $R_{load}$ . This exceptional output retention response for half an hour signifies the remarkable durability of the DLC film inherited from its  $sp^3$  character and low friction from its complimentary PTFE tribo- pair into the energy harvesting system. The output power density of  $141 \text{ mW m}^{-2}$  with remarkable durability highlights the potential of PTFE and DLC tribo- pair in low-frequency operating applications.

Moreover, the paper significantly contributes advancement of the fundamental understanding of the triboelectrification mechanism to design and better understand a tribo-interface of any energy harvesting system. This includes the influence and limitations of time required for the charge transfer, operating frequency, and gap between the tribo- materials in charge generation, storage, and transfer between the tribo- pairs and through the external circuit.

### 4. Experimental Section

**Synthesis of DLC through Pulsed-DC Magnetron Sputtering:** DLC deposition was carried out using a pulsed DC magnetron sputtering process shown in Figure 1a. Microwave plasma was used for chamber pre-cleaning. A combination of turbo (Osaka Vacuum 1500 l/s) and cryocooler water vapor pumping (IGG polycold) achieved vacuum pumping to a final system base pressure of  $5 \times 10^{-7}$  mbar. The deposition was carried out at an ambient temperature with Ar work gas and a high-purity C sputter target (purity 99.9995%). The deposition of 2- $\mu\text{m}$  thick DLC films was carried out by using an Ar flow of 100 sccm and a magnetron power of 46 kHz, resulting in a deposition rate of  $0.023 \text{ nm s}^{-1}$ .

**Characterization of DLC Material:** X-ray photoelectron spectroscopy (XPS) was carried out using a Specs Phoibos 100 MCD-5 hemispherical analyzer with 5 single channel electron multipliers. The non-monochromatic Specs XR-50 X-ray source with Mg K $\alpha$  (1253.6 eV) radiation was used for the collection of the low energy resolution scans (survey scans) over a wide energy range of 1200 eV with a step of 1 eV. Moreover, high-resolution scans with a step of 0.1 eV were performed for the investigation of specified regions of interest (C1s and O1s). XPS spectra were analyzed using CasaXPS software (v.2.3.24PR1.0).

Raman measurements were taken with a Thermo Scientific DXR Raman microscope, equipped with a 532 nm laser, a 900 line/mm diffraction grating, laser power of 5.0 mW, silicon substrate serving as a reference, and a 100 $\times$  objective. Data was collected using the auto-exposure mode, with a signal-to-noise ratio of 100:1 and integration times of up to 5 min for each measurement. Python software was used to achieve Gaussian peak-fitting, and Raman intensity was obtained following peak deconvolution.

Optical properties of DLC films, including transmittance ( $T$ ) and reflectance ( $R$ ) have been analyzed by spectrophotometry (UV-VIS-IR spectrophotometer, NKD-8000 from Aquila Instruments) for wavelengths ranged between 340 nm to 1.7  $\mu\text{m}$ , and by FTIR (Thermo Fisher Scientific Nicolet iS50) for wavelengths ranged between 2 and 25  $\mu\text{m}$ . Band gap

energy ( $E_p$ ) of the DLC films was obtained from Tauc's plot (Figure 1b) as thoroughly described in Supporting Information.

**Characterization of DLC-PTFE based TENG:** For electrical characterization of TENG, a home-made automatic actuation system was used as shown in Figure 2a. A Cu tape was attached to the entire surface of a  $40 \times 40 \text{ mm}^2$  PTFE film with a thickness of  $100 \mu\text{m}$ , forming the conductive electrode of the first triboelectric material. Then, PTFE film was attached to a vertical platform mounted on an X-Y stage fixed to an optical table. The second triboelectric material (i.e., DLC film deposited on Al foil) was attached to a dynamic plate mounted on a linear motor with a stroke of  $100 \text{ mm}$  and a maximum force of  $22 \text{ N}$  (DM01-23x80F-HP-H-100\_MS13 from Quinn systems). A BNC cable was soldered to electrodes of each triboelectric material (i.e., Al and Cu for the DLC and PTFE, respectively). That cable was connected to a fixture box capable to function either in voltage or current modes (see Figure 2a). In voltage mode, the output of the box was connected to an oscilloscope (DSOX4024A Oscilloscope from Keysight) through a  $100 \text{ M}\Omega$  input impedance probe (BKPR2000B-ND from B&K Precision), ensuring the accurate measurement of the  $V_{oc}$  and the voltage drop in a  $R_{load}$ . In the current mode,  $I_{sc}$  was measured using an electrometer with an input impedance above  $200 \text{ T}\Omega$  and a resolution of  $0.01 \text{ fA}$  (B2985A Electrometer from Keysight); this mode also allowed measuring the current electric flowing through a  $R_{load}$  and an energy storage device (e.g., a capacitor). The electrometer was connected to GPIB converter which in turn was connected to the computer via USB and interfaced through NI Labview (version 13.0), allowing the measurement of TENG electric properties as a function of time and for various contact-separation frequencies, and gaps between triboelectric materials. In addition, this program was used to study the charging characteristics of a  $3.3 \mu\text{F}$  capacitor as a function of the contact-separation parameters (i.e., frequency and approaching gap distance).

## Supporting Information

Supporting Information is available from the Wiley Online Library or from the author.

## Acknowledgements

This work was funded by the British Council & Higher Education Commission (20-ICRG-165/RGM/HEC/2020).

## Conflict of Interest

The authors declare no conflict of interest.

## Data Availability Statement

The data that support the findings of this study are available from the corresponding author upon reasonable request.

## Keywords

band-to-band charge transfer, DLC, magnetron sputtering, mechanical energy harvesting, triboelectric nanogenerators

Received: March 22, 2023  
Revised: June 23, 2023  
Published online: July 4, 2023

[1] N. Hossein Motlagh, M. Mohammadrezaei, J. Hunt, B. Zakeri, *Energies* **2020**, *13*, 494.

- [2] C. Qiu, F. Wu, C. Lee, M. R. Yu, *Nano Energy* **2020**, *70*, 104456.
- [3] F.-R. Fan, Z.-Q. Tian, Z. Lin Wang, *Nano Energy* **2012**, *1*, 328.
- [4] C. Xu, B. Zhang, A. Wang, W. Cai, Y. Zi, P. Feng, Z. Wang, *Adv. Funct. Mater.* **2019**, *29*, 1903142.
- [5] X. Ma, S. Li, S. Dong, J. Nie, M. Iwamoto, S. Lin, L. Zheng, X. Chen, *Nano Energy* **2019**, *66*, 104090.
- [6] J. Zhou, J. Zhang, Y. Deng, H. Zhao, P. Zhang, S. Fu, X. Xu, H. Li, *Nano Energy* **2022**, *99*, 107411.
- [7] S. Sharma, R. Kiran, P. Azad, R. Vaish, *Energy Convers Manag* **2022**, *254*, 115272.
- [8] C. Song, X. Zhu, M. Wang, P. Yang, L. Chen, L. Hong, W. Cui, *Sustain. Energy Technol. Assess.* **2022**, *53*, 102767.
- [9] P. Carneiro, M. P. Soares dos Santos, A. Rodrigues, J. A. F. Ferreira, J. A. O. Simões, A. T. Marques, A. L. Kholkin, *Appl. Energy* **2020**, *260*, 114191.
- [10] A. Babu, I. Aazem, R. Walden, S. Bairagi, D. M. Mulvihill, S. C. Pillai, *Chem. Eng. J.* **2023**, *452*, 139060.
- [11] J. Shen, B. Li, Y. Yang, Z. Yang, X. Liu, K.-C. Lim, J. Chen, L. Ji, Z.-H. Lin, J. Cheng, *Biosens. Bioelectron.* **2022**, *216*, 114595.
- [12] D. Deepak, N. Soin, S. S. Roy, *Mater. Today Commun.* **2023**, *34*, 105412.
- [13] Y. Qin, W. Zhang, Y. Liu, J. Zhao, J. Yuan, M. Chi, X. Meng, G. Du, C. Cai, S. Wang, S. Nie, *Nano Energy* **2023**, *106*, 108079.
- [14] M. Minagawa, T. Saito, Y. Fujikura, T. Watanabe, H. Iwabuchi, F. Yoshii, T. Sasaki, *J. Appl. Polym. Sci.* **1997**, *63*, 1625.
- [15] S. Lee, Y. Lee, D. Kim, Y. Yang, L. Lin, Z.-H. Lin, W. Hwang, Z. L. Wang, *Nano Energy* **2013**, *2*, 1113.
- [16] K. Anlin Lazar, K. V. Vijoy, T. Joseph, H. John, K. J. Saji, *Mater. Sci. Eng. B* **2023**, *292*, 116388.
- [17] C. Luo, Y. Shao, H. Yu, H. Ma, Y. Zhang, L. Gu, B. Yin, M. Yang, *Chem. Phys. Lett.* **2023**, *813*, 140276.
- [18] G. I. Dzhardimalieva, B. C. Yadav, T. V. Lifintseva, I. E. Uflyand, *Eur. Polym. J.* **2021**, *142*, 110163.
- [19] Z. L. Wang, *ACS Nano* **2013**, *7*, 9533.
- [20] G. Zhu, Z.-H. Lin, Q. Jing, P. Bai, C. Pan, Y. Yang, Y. Zhou, Z. L. Wang, *Nano Lett.* **2013**, *13*, 847.
- [21] S. H. Ramaswamy, J. Shimizu, W. Chen, R. Kondo, J. Choi, *Nano Energy* **2019**, *60*, 875.
- [22] A. Hirsch, *Nat. Mater.* **2010**, *9*, 868.
- [23] K. Sakurai, M. Hiratsuka, H. Nakamori, K. Namiki, K. Hirakuri, *Diam Relat Mater* **2019**, *96*, 97.
- [24] F. Atchison, T. Bryś, M. Daum, P. Fierlinger, A. Foelske, M. Gupta, R. Henneck, S. Heule, M. Kasprzak, K. Kirch, R. Kötz, M. Kuźniak, T. Lippert, C.-F. Meyer, F. Nolting, A. Pichlmaier, D. Schneider, B. Schultrich, P. Siemroth, U. Straumann, *Diam Relat Mater* **2007**, *16*, 334.
- [25] J. C. Ding, M. Chen, H. Mei, S. Jeong, J. Zheng, Y. Yang, Q. Wang, K. H. Kim, *Diam Relat Mater* **2022**, *123*, 108861.
- [26] J. H. Kim, S. Kang, J.-W. Park, E.-D. Park, Y.-K. Jun, J. Y. Han, J. H. Jung, N. Kim, G.-H. Lee, *ACS Appl. Electron. Mater.* **2021**, *3*, 1771.
- [27] V.-M. Tiainen, A. Soininen, E. Alakoski, Y. T. Konttinen, *Diam Relat Mater* **2008**, *17*, 2071.
- [28] J. Vyskočil, P. Mareš, Z. Hubička, M. Čada, T. Mates, *Surf. Coat. Technol.* **2022**, *446*, 128765.
- [29] A. Hu, M. Rybachuk, Q.-B. Lu, W. W. Duley, *Diam Relat Mater* **2008**, *17*, 1643.
- [30] W. Wu, Z. Zhu, J. Min, J. Zhang, N. Qian, M. Jiang, *Thin Solid Films* **2017**, *622*, 89.
- [31] W. Yu, J. Zhang, X. Liu, W. Xi, *Diam Relat Mater* **2003**, *12*, 2203.
- [32] N. Aslan, M. Ş. Kurt, M. Mehmet Koç, *Opt. Mater.* **2022**, *126*, 112229.
- [33] D. Gibson, S. Song, L. Fleming, S. Ahmadzadeh, H. O. Chu, S. Sproules, R. Swindell, X. Zhang, P. Navabpour, C. Clark, M. Bailey, *Appl. Opt.* **2020**, *59*, 2731.

- [34] S. Ahmadzadeh, D. Gibson, L. Fleming, D. Hutson, S. Song, A. James, S. Wells, A. Forsyth, S. Bruckshaw, *Appl. Opt.* **2023**, 62, B79.
- [35] D. Gibson, D. Hutson, S. Song, GB2592094A, <https://patentimages.storage.googleapis.com/ec/38/83/8ce3138ab55561/GB2592094A.pdf> (accessed: 18 August, **2021**).
- [36] D. Gibson, S. Song, WO2018197867A1, <https://patentimages.storage.googleapis.com/ae/d1/4a/5c8db984ec25bb/WO2018197867A1.pdf> (accessed: 01 November, **2018**).
- [37] I.-W. Tcho, W.-G. Kim, S.-B. Jeon, S.-J. Park, B. J. Lee, H.-K. Bae, D. Kim, Y.-K. Choi, *Nano Energy* **2017**, 42, 34.
- [38] N. Wang, W. Zhang, Z. Li, S. Wang, A. Suwardi, E. Ye, B. Li, Y. Liu, Z. Wu, Y. Dong, X. J. Loh, D. Wang, *Nano Energy* **2022**, 103, 107748.
- [39] R. Ouyang, Y. Huang, H. Ye, Z. Zhang, H. Xue, *Nano Energy* **2022**, 102, 107749.
- [40] Z. B. Li, H. Y. Li, Y. J. Fan, L. Liu, Y. H. Chen, C. Zhang, G. Zhu, *ACS Appl. Mater. Interfaces* **2019**, 11, 20370.
- [41] H. Zou, Y. Zhang, L. Guo, P. Wang, X. He, G. Dai, H. Zheng, C. Chen, A. C. Wang, C. Xu, Z. L. Wang, *Nat. Commun.* **2019**, 10, 1427.
- [42] N. Cui, L. Gu, Y. Lei, J. Liu, Y. Qin, X. Ma, Y. Hao, Z. L. Wang, *ACS Nano* **2016**, 10, 6131.
- [43] A. Tibrewala, E. Peiner, R. Bandorf, S. Biehl, H. Lüthje, *Appl. Surf. Sci.* **2006**, 252, 5387.
- [44] M. Wang, J. Duan, X. Yang, Y. Wang, Y. Duan, Q. Tang, *Nano Energy* **2020**, 73, 104747.
- [45] N. Paik, *Surf. Coat. Technol.* **2005**, 7, 2170.
- [46] T. R. Gengenbach, G. H. Major, M. R. Linford, C. D. Easton, *J Vac Sci Technol A* **2021**, 39, 013204.
- [47] A. Ejaz, J. H. Han, R. Dahiya, *J. Colloid Interface Sci.* **2020**, 570, 322.
- [48] B. Lesiak, L. Kövér, J. Tóth, J. Zemek, P. Jiricek, A. Kromka, N. Rangam, *Appl. Surf. Sci.* **2018**, 452, 223.
- [49] S. Kaciulis, *Surf. Interface Anal.* **2012**, 44, 1155.
- [50] J. F. Morar, F. J. Himpsel, G. Hollinger, J. L. Jordan, G. Hughes, F. R. McFeely, *Phys. Rev. B* **1986**, 33, 1340.
- [51] Y. Mizokawa, T. Miyasato, S. Nakamura, K. M. Geib, C. W. Wilmsen, *J. Vac. Sci. Technol. Vac. Surf. Films* **1987**, 5, 2809.
- [52] L. Stobinski, B. Lesiak, A. Malolepszy, M. Mazurkiewicz, B. Mierzwa, J. Zemek, P. Jiricek, I. Bielowshapka, *J. Electron Spectrosc. Relat. Phenom.* **2014**, 195, 145.
- [53] S. T. Jackson, R. G. Nuzzo, *Appl. Surf. Sci.* **1995**, 90, 195.
- [54] Yu. V. Butenko, S. Krishnamurthy, A. K. Chakraborty, V. L. Kuznetsov, V. R. Dhanak, M. R. C. Hunt, L. Šiller, *Phys Rev B Condens Matter Mater Phys* **2005**, 71, 075420.
- [55] Y.-S. Li, S. Jang, A. Khan, T. Martin, Q. J. Wang, A. Martini, Y.-W. Chung, S. H. Kim, *Do DLC-like features in Raman spectra of tribofilms really mean they are DLC formed by friction?*, In Review, **2022**.
- [56] D. Martinez-Martinez, M. Schenkel, Y. T. Pei, J. C. Sánchez-López, J. Th. M. De Hosson, *Surf. Coat. Technol.* **2011**, 205, S75.
- [57] W. G. Cui, Q. B. Lai, L. Zhang, F. Wang, *Surf. Coat. Technol. – SURF COAT TECH* **2010**, 205, 1995.
- [58] A. C. Ferrari, J. Robertson, *Phys. Rev. B* **2001**, 64, 075414.
- [59] A. C. Ferrari, B. Kleinsorge, N. A. Morrison, A. Hart, V. Stolojan, J. Robertson, *J. Appl. Phys.* **1999**, 85, 7191.
- [60] A. C. Ferrari, S. E. Rodil, J. Robertson, *Phys. Rev. B* **2003**, 67, 155306.
- [61] M. Chhowalla, A. C. Ferrari, J. Robertson, G. A. J. Amarantunga, *Appl. Phys. Lett.* **2000**, 76, 1419.
- [62] B. K. Tay, X. Shi, H. S. Tan, D. H. C. Chua, *Surf. Interface Anal.* **1999**, 28, 231.
- [63] B. K. Tay, X. Shi, H. S. Tan, H. S. Yang, Z. Sun, *Surf. Coat. Technol.* **1998**, 105, 155.
- [64] A. C. Ferrari, J. Robertson, *Phys. Rev. B* **2000**, 61, 14095.
- [65] D. N. G. Krishna, J. Philip, *Appl. Surf. Sci. Adv.* **2022**, 12, 100332.
- [66] L. Opilik, T. Schmid, R. Zenobi, *Annu. Rev. Anal. Chem.* **2013**, 6, 379.
- [67] D. He, X. Zhang, Q. Yang, M. Z. Atashbar, *Chem. Eng. J.* **2023**, 456, 141012.
- [68] A. R. Mule, B. Dudem, H. Patnam, S. A. Graham, J. S. Yu, *ACS Sustainable Chem. Eng.* **2019**, 7, 16450.
- [69] Z. L. Wang, A. C. Wang, *Mater. Today* **2019**, 30, 34.
- [70] S. Lin, L. Xu, C. Xu, X. Chen, A. C. Wang, B. Zhang, P. Lin, Y. Yang, H. Zhao, Z. L. Wang, *Adv. Mater.* **2019**, 31, 1808197.
- [71] Z. You, S. Wang, Z. Li, Y. Zou, T. Lu, F. Wang, B. Hu, X. Wang, L. Li, W. Fang, Y. Liu, *Nano Energy* **2022**, 91, 106667.
- [72] M. Kim, S. H. Kim, M. U. Park, C. Lee, M. Kim, Y. Yi, K.-H. Yoo, *Nano Energy* **2019**, 65, 104079.
- [73] Y. Xu, G. Min, N. Gadegaard, R. Dahiya, D. M. Mulvihill, *Nano Energy* **2020**, 76, 105067.
- [74] S. Wang, Y. Xie, S. Niu, L. Lin, C. Liu, Y. S. Zhou, Z. L. Wang, *Adv. Mater.* **2014**, 26, 6720.
- [75] C. Zhang, L. Zhou, P. Cheng, X. Yin, D. Liu, X. Li, H. Guo, Z. L. Wang, J. Wang, *Appl. Mater. Today* **2020**, 18, 100496.
- [76] D. Liu, L. Zhou, S. Cui, Y. Gao, S. Li, Z. Zhao, Z. Yi, H. Zou, Y. Fan, J. Wang, Z. L. Wang, *Nat. Commun.* **2022**, 13, 6019.
- [77] W. Tang, C. Zhang, C. B. Han, Z. L. Wang, *Adv. Funct. Mater.* **2014**, 24, 6684.